ICAS-88-2.4.4

EXPERIMENTAL AND NUMERICAL STUDY OF PROPELLER WAKES IN AXIAL FLIGHT REGIME

D. Favier*, A. Ettaouil**, C. Maresca+ and C. Barbi‡

Institut de Mécanique des Fluides
Université d'Aix-Marseille II, UM-34 du C.N.R.S.
1, rue Honnorat 13003 Marseille, France

Abstract

An experimental and numerical investigation of the axial flight regime of a propeller operating either in the isolated configuration or in the propeller/nacelle/wing combination is described in the paper. For the isolated propeller configuration the numerical approach is based on a free wake analysis code which uses a complete equilibrium procedure for the wake influence calculation. The code prediction efficiency is checked by comparison with experimental data obtained on both the overall propeller performances and the associated 3D wake velocity field. In the interaction case a series of wind tunnel experiments is performed on each component of the propeller/nacelle/wing configuration in order to characterize the net influence of the propeller slipstream on the wing aerodynamic behavior. Overall lift, drag and moment coefficients as well as chordwise pressure distributions are measured at different spanwise sections of the wing. These experimental data are compared with the numerical results obtained by coupling the free wake analysis code for the slipstream and a panel method for the fixed wing.

Nomenclature

α	Geometric incidence of the propeller/nacelle/wing configuration, (deg)
α_0	Mean pitch angle at $\xi = 0,7$ of the propeller blade, (deg)
α_1	Wing geometric incidence with the propeller axis ($\alpha_1 = -2°$)
α_k	Coefficients of the Fourier series of the circulation Γ
b	Number of blades (b = 4)
χ	Propeller power coefficient, ($\chi = P/\rho\, n^3 D^5$)
c	Wing chord section c = 1.2D = 1.02 m
Q	Propeller torque (N.m)
C_D	Drag coefficient of the wing, ($C_D = D/1/2\, \rho\, V_\infty^2\, S$)
C_L	Lift coefficient of the wing, ($C_L = L/1/2\, \rho\, V_\infty^2\, S$)
C_M	Moment coefficient of the wing, ($C_M = M/1/2\, \rho\, V_\infty^2\, S\, c$)
C_p	Pressure coefficient, ($C_p = (p-p_\infty)/1/2\, \rho\, V_\infty^2$)
C_T	Traction coefficient of propeller/nacelle/wing, ($C_T = T/1/2\, \rho\, V_\infty^2\, S$)
D, D_0	Propeller diameter (D = 0.85 m) and hub diameter (D_0 = 0.14 m)
γ	Propeller operating parameter, ($\gamma = V_\infty / nD$)
Kp	Total pressure jump coefficient through the rotating plane, ($K_p = (p_{t2}-p_{t1})/\rho n^2 D^2$)
λ	Propeller advance ratio, ($\lambda = V_\infty/\omega R = \gamma/\pi$)
L	Wing span, (L=2D=1.70m)
M	Pitching moment of the wing, (N.m)
ν	Kinematic viscosity, N/(m.sec)
n	Propeller rotating frequency, (rps)
OXYZ	Fixed coordinates system defined in Figure 2b
P	Propeller power, ($P = 2\pi n Q$), (Watt).
p, p_t	Static and total pressure, (Pa)
p_∞	Pressure at infinity, (Pa)
R	Propeller radius, R=D/2, (m)

---

* CNRS Research Scientist, AIAA Member
** IMFM Graduate Student
\+ CNRS Senior Research Scientist, AIAA Member
‡ CNRS Research Scientist

r	Radial coordinate from the axis of rotation, (m)
ρ	Specific density of air, (Kg/m^3)
S	Wing surface, S=Lc, (m^2)
t	Time, (s)
T	Propeller thrust , (N)
τ	Propeller thrust coefficient, ($\tau = T/\rho\, n^2\, D^4$)
U,V,W	Velocity components defined in Figure 2b, (m/s)
V_∞	Velocity at infinity, (m/s)
Ω, ω	Propeller rotational frequency, (rad/s)
ωt	Phase of the period, (deg).
ξ	Reduced coordinate along the blade radius, ($\xi = r/R$)
ψ	Azimuthal blade position, ($\psi=\Omega t$) (deg)
ψ_S	Azimuth of the far wake position, (deg)

subscripts

∞	Relative to uniform flow conditions
i,ind	Relative to induced quantities

Introduction

The rotary wings performances and the interference effects with other aircraft components demand nowadays to be accurately determined and are still a challenge for aerodynamicists. This is specially true for recent highly-loaded propellers (1,2,3) or tilted-rotor configurations (4,5) in order to improve the design and the installation of the propulsion system. As reported in references 6-9, a proper study of the interference problem requires to quantify both the influence of the slipstream on the downstream aircraft structures which can produce an increase in drag and a span loading disturbance on wing and fuselage; and reciprocally the influence of these structures on the rotary wings flowfield which can degrade the installed performance of the propulsion system.

However the interference problem remains complex as a whole and is usually tackled in two successive steps of investigation. The first approach consists in studying the configuration of isolated rotary wings operating in different flight conditions. For example, references 10-15 illustrate some experimental and numerical studies conducted on rotors and propellers flowfields. For this isolated configuration, computer codes are generally based on free wake analysis (FWA) models. The FWA solution involves an iterative process on the wake geometry until the velocity field is consistent with local blade circulation and the overall thrust coefficient. Most of the computer codes are checked by comparison with either overall or local experimental data bases. Very few studies have considered both the overall performances and the local velocity data to evaluate the code efficiency. However, interference problems imply a correct prediction of both the blade airloads distribution and the complete downstream flowfield.

In the second approach, experiments are conducted on multi-components configurations including propeller, nacelle, wing and flaps (see references 6, 9, 16, 17). In such wind tunnel tests, the net interaction effects can only be obtained when the instrumented model is design in such a way that the contributions of each component can be measured and quantified. A special attention should also be paid to the walls effect of the wind tunnel in the case of closed test sections (9). Concerning the numerical aspects, only the slipstream influence on the downstream structures, generally modeled using panel methods, has been mainly investigated. Very few studies simultaneously solve the rotary wing model and the interacted structure model to account for their mutual influence (6).

The present paper is concerned with some of the points previously raised and is divided in two parts. The first objective is to develop an efficient code based on the free wake analysis calculation in the case of the isolated propeller configuration. The FWA code involves a complete equilibrium procedure (both on the tip vortex and vortex sheet filaments) and its predictions efficiency is checked by comparison with a wide experimental data base obtained on a conventional four-bladed propeller operating at subsonic speeds. The code validation includes comparisons with both overall performances and local instantaneous 3D velocity field measured at several downstream distances of the rotating plane.

In the second part of the paper, the objective is to evaluate the influence of the propeller slipstream (modeled with the previous FWA code) on a downstream wing modeled using a panel method. The configuration consists in a fixed wing joined by a nacelle to the previous four-bladed propeller. Here again the code validation is achieved by comparisons with overall wing airloads as well as chordwise pressure distributions measured at different sections along the wing span. The wind tunnel model is design to obtain the net mutual interference effects as deduced from a series of measurements realized in successive configurations of the 3 elements: propeller, nacelle and wing. Instantaneous effects obtained on the pressure distributions as a function of the blade azimuth are also analyzed and compared to the unsteady mean effects generated by the slipstream over a rotational period.

Experimental facilities and measurement techniques

The experiments are conducted at I.M.F.M. in the S1 subsonic open circuit wind-tunnel : open elliptical test section 3.3 x 2.2 m^2, length 3 m, maximum freestream velocity V_∞ = 50 m/s. The installations used to simulate the isolated propeller flowfield and the propeller/nacelle/wing interference problem are given in Figure 1a,b. The isolated propeller shown in Figure 1a is a four bladed model of diameter D = 0.85m (hub diameter : D_0 = 0.14m). The blade is generated by the NACA 64A408 airfoil series with an evolutive chord distribution and a non linear twist law defined in reference 11. In this case the propeller is mounted without any nacelle on a cylindrical supporting mast which contains the driving shaft and transmission system. Figure 1b presents the propeller/nacelle/wing configuration where the propeller is the same as in Figure 1a and is powered by an electrical motor housed within the nacelle.

As shown in Figure 1a,b the same mast is used to support either the isolated propeller or the wing and its nacelle for the interaction configuration. The mast is equipped with a set of 12 strain-gauges mounted in Wheastone bridges combinations for the purpose of airloads components and pitching moments measurements. The strain-gauges system provides either the thrust and power coefficients (τ,χ) of the propeller in the isolated configuration, or the overall lift, drag or thrust, and pitching moment coefficients (C_L, C_D or C_T, C_M) of the propeller/nacelle/wing ensemble, considered as a whole or as dissociated elements of the interaction set-up. For this last configuration, the power coefficient χ is measured separately by an additional torquemeter housed in the nacelle.

Figure 2a,b sketches side and top views of the propeller/nacelle/wing configuration. The nacelle/wing, shown in Figure 2a, is a scaled model of the actual ensemble installed on the Aérospatiale ATR-42 commuter airplane. The wing has a constant RA1843N1L1 airfoil section of 17% for maximum thickness. A negative angle α_1 = -2° is fixed between the line chord of the airfoil and the propeller axis in order to respect the actual aircraft design. All the geometrical parameters of the wind tunnel model defined in Figure 2a are representative of the actual ATR-42 configuration except the distance d, between the rotating plane and the leading edge of the wing which is reduced by a factor 1/2 in the wind tunnel simulation. The propeller/nacelle/wing ensemble can also be rotated around the mast axis. The angle of attack between the propeller axis and the freestream direction V_∞ is noted α in Figure 2a, and is fixed at α = 0° for all the tests presented in this paper.

The top view in Figure 2b shows that the rectangular wing (1.70 x 1.02 m^2) is composed of three parts and limited on both sides by end plates in order to minimize the 3D flow effect at the outboard sections of the wing. The central part of the wing (0.20 x 1.02 m^2) is linked with the nacelle and the propeller by means of two connecting profiles on each side. These connections allow either the coupling or the uncoupling of the wing with the rest of the ensemble, and thus provide the propeller performances when the wing is present but not weighted by the strain-gauges system. More details on this measurement procedure can be found in reference 19.

The two other parts of the wing model 2 x (0.75 x 1.02 m^2) can be interchanged from the up-going blade side to the down-going blade side as depicted in Figure 2b. On one side the wing is in fact made of a stack of small elements tightened together by traversing rods. One of them (100 mm width) is equipped with 20 Endevco pressure transducers distributed along the airfoil chord on the upper and lower side. Another one is instrumented with 20 hot film gauges mounted flush on the upper and lower surface. The chordwise pressure and skin friction distributions are then obtained at different stations X/(L/2) = constant (sections numbered from 1 to 5 for the up-going blade side in Figure 2b) by displacing the instrumented airfoil section along the wing span.

In the isolated airfoil configuration, the primary objective of the study is to constitute an experimental data base appropriate for checking the computer code prediction. To this end, the isolated propeller flowfield has been preliminary investigated over a wide range of blade pitch angles ($23° \le \alpha_0 \le 32.5°$) and operating parameters ($0.2 \le \gamma \le 1.1$) of the axial flight regime. The measuring techniques used in this experimental investigation are reported in references 11,12 and 18-20. This includes strain-gauges technique for overall data, smoke visualizations, Laser velocimetry and X-hot wire anemometry for surveying the flow near the blades, in the middle and far wake regions. The available tests data concerning the isolated propeller case therefore include overall and local aerodynamic quantities. The τ and χ coefficients of the propeller have been determined for operating conditions varying from zero thrust level to the maximum thrust regime (near stall). The tip vortex path (r_t, Z_t) as well as the far wake position ψ_s are given by synthesized formulations as function of the blade azimuth position ψ and the α_0 and γ parameters (see

references 18-20). The 3D instantaneous velocity U = U(ψ), V = V(ψ), W = W(ψ) defined in Figure 2b have been determined in several planes Z/R = constant downstream of the rotating disk. As a function of the reduced blade radius ξ and azimuth ψ, each velocity component is also reduced to a 10th order Fourier series in the form :

$$U(\xi, \psi) = U_0 + \sum_{n=1}^{10} U_n \cos(n\psi + \Phi_n)$$

For the propeller/nacelle/wing interaction study, static pressure and skin friction measurements on the wing are added to the previous techniques to document the slipstream influence on the wing. Reciprocally, the effect induced by the nacelle/wing ensemble on the propeller is measured by total pressure probing displaced upstream and downstream of the propeller disk along a diameter parallel to the wing span. In order to obtain the induced effect on each element, a series of airloads and moment measurements on various flow configurations (propeller + nacelle + wing, propeller + nacelle + wing uncoupled, propeller + nacelle, wing alone, ...) has to be performed. The resulting data are algebraically combined in a manner suitable for extracting the net interaction influence on the wing forces and moment and also on the propeller performances. The complete procedure is detailed in references 19,20.

Calculations methods and numerical procedures

The so called SMEHEL program solves the isolated propeller flowfield case and uses a lifting line model to represent each propeller blade. N_p = 11 calculation points are defined along this line which is located at the quarter chord axis. The wake is formed by a finite number (N_L = 12) of trailing vortex filaments shed from each blade between two calculation points as shown in Figure 3. The last filament represent the tip vortex line. The inboard sheet (i = 1 to 11) plus the tip vortex (i = 12) form the near free wake. The far wake region is represented by semi-infinite cylinders of constant vorticity attached to each free wake filament. The end of the free wake is obtained at the azimuth ψ_S given (11) by

$$(\psi_S - \psi_b)/(b \cdot \psi_b) = 1/4\{8.5 - \alpha_0/10 - \gamma(2 + \gamma)\}$$

The initial inboard sheet position and the tip vortex are known from experimental synthesized formulations given in references 11 and 12. An equilibrium calculation (condition of tangency of the velocity to the vortex filament) is performed on the inboard vortex sheet and the tip vortex as shown on the block diagram in Figure 4. The resolution process begins with an estimation of the coefficients α_k of the circulation Fourier series by considering the flow through the propeller disk without any wake influence. To start, the calculation needs : the geometrical conditions and flight operating parameters b, α_0, θ_v, and V_∞, Ω, γ, λ. All the calculations are performed in a frame rotating with the blades.

The propeller/wing interaction program, so called COHV, is an extension of SMEHEL since the isolated propeller code gives the complete unsteady 3D flowfield at any downstream plane Z/R=constant when convergence and equilibrium conditions are reached. This wake flowfield is then used as a boundary condition of the panel method that describes the surface of the downstream wing. The 3D propeller wake induces in all the space velocity and swirl added to the uniform flowfield (see Figure 5). Before tackling the complex interaction flowfield as a whole, it is followed here a simplified approach by neglecting the influence of the wing on the propeller and by considering the wing as embedded in the slipstream of the isolated propeller. With these assumptions, the potential φ can be expressed as the sum of the contribution of the uniform flow φ_∞, the wake φ_S and the wing potential of perturbation φ_W

$$\varphi(x,y,z,t) = \varphi_\infty + \varphi_S(x,y,z,t) + \varphi_W(x,y,z,t).$$

The associated velocity field is then

$$V(x,y,z,t) = V_\infty + V_S(x,y,z,t) + \mathrm{grad}(\varphi_W(x,y,z,t)).$$

The potential φ is obtained solving the Laplace equation $\Delta(\varphi(x,y,z,t)) = 0$.

The wing is represented by singularities distributed on a 20x20 mesh on each side of the surface as shown in Figure 5. On the panels, singularities made of doublets are calculated at each phase ψ of the rotational period. The coupling between the propeller slipstream and the wing is obtained by imposing a Neuman condition on the wing surface. The wing has its own wake modeled as a plane surface with a similar mesh and singularity distribution than the wing itself.

Figure 6 gives the block diagram of the COHV code. The parametric flow conditions and geometrical configuration on wing and propeller are first given . Then, the interaction option of the code can be selected and steps 0 and 1 of the SMEHEL procedure solves the 3D velocity flowfield induced

in the slipstream which is added to the freestream velocity V_∞ as a function of the blade azimuth ψ. If the isolated wing option is selected, no slipstream influence is taken into account and the wing aerodynamics are calculated in the uniform flow alone. The results of isolated and interacted wing configurations can therefore be compared by using the two previous options.

From the instantaneous velocity field generated using the SMEHEL procedure, the intensities of the doublet singularities are determined at each control points of the wing surface (step 2a in Figure 6). The own vortex sheet influence of the wing is also added in step 2b. The calculation of the matrix influence coefficients then gives the local velocity field on the whole wing surface for each time step of the blade rotation. Local and global wing airloads and moment, circulation distribution as well as chordwise pressure distributions at different sections of the span are finally obtained as output of the model.

Isolated propeller configuration results

In order to build confidence in the computer code SMEHEL, the predicted overall performances and local 3D velocity field are compared with the experimental data over a wide range of operating parameters of the axial flight regime. Concerning the overall performances, Figures 7a-c present the calculated thrust coefficient τ superimposed to the measured data taken from reference 12, for increasing values of the mean pitch angle α_0. The results generally indicate a good correlation calculation/ experiment. For all the cases shown in Figure 7a-c, the τ correlation with the measured values is better than 4%. The best results are shown to be obtained at the highest pitch angle value $\alpha_0 =$ 32.5° (prediction better than 1%). The relatively stronger discrepancy appears for $\alpha_0 = 27°$ at the lowest values of the operating parameter γ. The calculated power coefficients χ presented in Figures 8a-c also show a good agreement with experiments. However, a tendency to slightly underestimate the experimental propeller power is observed for $\gamma \geq$ 0.7. It can be noticed that the direct comparison between calculation code predictions and experimental results is possible (20) because the FWA procedure SMEHEL does not require any change of the initial mean pitch angle value α_0.

Since the details of the wake flowfield streaming back of the propeller is of primary importance in the interference problem, the comparison of the code predictions versus experiments have been extended to the instantaneous 3D velocity field obtained at several downstream distances of the rotating plane. As an example Figures 9, 10 and 11 present the calculated and measured evolution of the velocity components U, V, W, reduced by V_∞, as a function of the reduced blade radius ξ for the parametric conditions $\alpha_0 =$ 32.5° ; $\gamma = 0.89$; Z/R = 0.203, and at four azimuthal blade positions ψ= 15°, 35°, 45° and 75°.

The tip vortex crossing with this downstream plane, relatively close to the blade (Z/R = 0.203), is occurring at $\xi = 0.97$ and $\psi = 37°$. The dependence of the velocity variations on the azimuth is clearly exhibited near the azimuth $\psi = 37°$ on all components and specially on the radial velocity profile U/U_∞ of Figure 9. In this Figure, the rapid evolution of the radial velocity component is well predicted by the calculation results at the four azimuthal values considered. Even in the vicinity of the tip vortex crossing, the decrease of radial velocity (at $\psi = 35°$) followed by a sharp increase (at $\psi = 45°$) is correctly correlated. The sole exception being near the blade root region and must be attributed to the fact that the hub geometry is not modeled in the present calculation.

These trends are also found on the reduced tangential component V/V_∞ in Figure 10 where a slight overestimation of the measured velocity levels appears in the prediction for $\psi \geq 45°$. Moreover, the agreement between calculation and experiment on the axial component W/W_∞ is shown to be excellent in Figure 11. The typical tip vortex influence is well captured between the azimuths $\psi = 35°$ and $\psi = 45°$ in Figure 11. Similar good correlations between calculation and experiment have been also obtained for cross planes located far from the rotating plane (as far as Z/R=1.8) and thus confirm the efficiency of semi infinite vortex cylinders to modeled the far wake region.

Propeller/nacelle/wing configuration results

The series of tests conducted on the propeller/nacelle/wing configuration have provided quantitative data qualifying the wing influence on the propeller performances that cannot be calculated using the interaction code COHV, in its present state of development, since this influence is not yet modeled. The fixed wing influence is illustrated in Figure 12a,b where the τ and χ coefficients (measured with and without the wing) are plotted

versus the operating parameter γ for two values of the mean pitch angles $\alpha_0 = 27°$ and $\alpha_0 = 32.5°$. For each α_0 values, the presence of the fixed wing has for effect to increase the propeller thrust coefficient, in Figure 12a. The gain due to the fixed wing on the power coefficient χ is slightly less, in Figure 12b. The thrust and power coefficients induced by the wing on the propeller can be defined as

$\tau_{ind}=\tau_{wing} - \tau_{w/o\ wing}$ $\chi_{ind}=\chi_{wing} - \chi_{w/o\ wing}$

From results of Figure 12a,b and in the range of γ considered $0.7\leq\gamma\leq1$, the net interference effects due to the wing can then be evaluated by the following ratios

$$\frac{\tau_{ind}}{\tau_{w/o\ wing}} \approx 14\ \% \qquad \frac{\chi_{ind}}{\chi_{w/o\ wing}} \approx 8\%$$

It should be noted, that the propeller had to operate at a constant rotating frequency n, thus this increase of thrust and power results in an increase of power from the electric motor. As mentioned in reference 9 for the thrust coefficient, these induced effects on the τ and χ coefficients can be attributed to the straightening of the slipstream by the fixed wing which results in a portion of swirl being recovered in the overall performances.

Moreover, the measurements carried on the isolated propeller and on the propeller/nacelle configuration have shown on the one hand a reduction of the thrust coefficient due to the presence of the nacelle; and on the other hand no significant modification of the power coefficient when compared to the isolated case. In this configuration the propeller/nacelle alone does not benefit of the slipstream straightening effect (19).

Another quantification of the wing influence on the local propeller flowfield is obtained by considering the total pressure jump through the propeller disk also measured with and without the fixed wing. For both configurations the Figure 13a gives the mean pressure coefficient $\overline{K_p}$ (averaged over a rotational period) measured along a diameter X/R parallel to the wing span for $\alpha_0 = 32.5°$, γ = 0.89 and $V_\infty = 17.2$ m/s. The curve corresponding to the tests carried out without the wing shows that the $\overline{K_p}$ distributions obtained on each side are nearly symmetric with respect to the propeller axis except a cut of the maximum peak on the up-going blade side. Moreover, each part of the curve is centered around the span station $|X/R|=0.6$. In presence of the wing, the $\overline{K_p}$ distribution corresponding to the up-going blade side is significantly modified. An increase of the $\overline{K_p}$ is observed all along the semi-span of the wing and the maximum value then occurs near the section X/R = -0.5. On the down-going blade side the maximum of $\overline{K_p}$ remains nearly at the same level but is shifted outboard up to X/R = 0.67. The coefficient $\overline{K_{p\ ind}}$ defined as the difference between the two curves of Figure 13a is plotted as a function of X in Figure 13b. This induced pressure coefficient clearly shows that the positive effect on the up-going blade side is not balanced on the other side, where positive values are recovered for $X/R \geq 0.82$ on the down-going blade side. Moreover, the integration of these $\overline{K_{p\ ind}}$ distributions well matches the overall induced effects that can de deduced from Figure 12a,b.

The reciprocal influence of the slipstream on the airloads and moment coefficients of the fixed wing is deduced from the strain gauges measurements technique. As previously mentioned, the net interference effect induced by the slipstream on the wing is obtained as the algebraic result (sums and differences) of airloads and moments measurements performed in successive flow configurations.

The Figure 14a,b,c presents the induced lift, drag and pitching moment coefficients (C_{Li}, C_{Di}, C_{Mi}) as a function of the operating parameter γ. It can be noticed that the uniform flow contribution is already subtracted to obtain the values plotted in figure 14a,b,c. The induced coefficients (C_{Li}, C_{Di}, C_{Mi}) are also compared in this figure with the coefficients ($C_{L\infty}$,$C_{D\infty}$, $C_{M\infty}$) measured on the wing alone in the uniform flow V_∞. For the induced lift coefficient, Figure 14a indicates a slight decrease of C_{Li} compared to $C_{L\infty}$ when the thrust of the propeller is high ($\gamma < 0.9$). However the induced lift is nearly of the same order of $C_{L\infty}$ and mild interference effects are shown on the overall wing lift. For the induced coefficient C_{Mi} in Figure 14c, a slight nose up moment is observed around $\gamma = 0.7$, but the slipstream influence remains also moderated. In fact, it is on the induced drag coefficient C_{Di} presented in Figure 14b that the influence of the slipstream appears to be the more significant. The increase of C_{Di} observed at low values of γ is about five times the uniform value $C_{D\infty}$: for example $C_{Di}/C_{D\infty} = 4.7$ at $\gamma = 0.7$ and $\alpha_0 = 32.5°$. It can be also noticed that the values of C_{Di} are almost independent of the mean pitch angle α_0.

Concerning the mean pressure $\overline{C_p}$ averaged over the blade rotational period, a comparison between

the experimental distributions and the results deduced from the COHV code is given in Figure 15a,b. The upper and lower side distributions obtained at section 5 (X/(L/2) = - 0.18) is presented for the uniform flow configuration (Figure 15a), and at sections 1 and 5 (X/(L/2) = - 0.65, X/(L/2) = - 0.18) behind the up-going propeller blade (Figure 15b) for the parametric conditions: $\gamma = 0.89$; $\alpha_0 = 32.5°$; $V_\infty = 17.2$ m/s and $\alpha = 0°$.

The results indicate that the leading edge predictions generally overestimate the experimental values, even in the uniform flow conditions in Figure 15a. The mesh size may be responsible of this discrepancy in the leading edge and trailing edge regions. From Z/R ≈ 0.15 up to the chordwise station Z/R ≈ 0.7, the calculated $\overline{C_p}$ distribution matches fairly well the experiments, even at the section X/(L/2) = - 0.18 located near the nacelle. It can be noticed that the $\overline{C_p}$ distribution corresponding to X/(L/2) = - 0.65 is very similar to the one obtained in the uniform flow since this section is located at the outside boundary of the propeller slipstream.

For both sections considered (sections 1 and 5), an increase of the $\overline{C_p}$ minimum value is observed on the upper side of the wing when compared to the uniform flow case. This effect is more accentuated for the section X/(L/2) = - 0.18 located within the propeller slipstream. The suction peak calculated and measured on the lower side of the wing is shown to be reduced when passing from a zone of mild slipstream influence (X/(L/2) = -0.65) to a section completely immersed in the slipstream (X/(L/2) = - 0.18). One of the major slipstream influence is to increase the velocity and to introduce a swirl of the flowfield, which therefore locally modify the angle of the airfoil sections. This modification of the local angle of attack induces an increase of the upper side suction peak and a reduction of the lower side suction peak when compared to the uniform flow distribution (keeping in mind that the angle α_1 defined in Figure 2a is fixed at a negative constant value $\alpha_1 = - 2°$).

The Figures 16, 17, 18 exemplify the instantaneous slipstream influence on the wing surface. The instantaneous Cp distributions measured on the upper and lower sides of the wing are compared to the corresponding COHV calculation results at the three sections 5, 3, 1 along the wing span defined by : X/(L/2) = - 0.65, X/(L/2) = - 0.41, X/(L/2) = - 0.18. The propeller operating conditions are the same as above : $\gamma = 0.89$; $\alpha_0 = 32.5°$; $V_\infty = 17.2$ m/s and $\alpha = 0°$.

The experimental results indicate that outside of the slipstream (section 1, Figure 16) and near the propeller axis (section 5, Figure 18), the instantaneous Cp distributions are almost identical for the two azimuthal blade positions $\psi = 0°$ and $\psi = 45°$. Whereas they are significantly different near the edge of the wake (section 3, Figure 17). In this figure, when increasing the azimuth from $\psi = 0°$ to $\psi = 45°$ at section 3, the upper side suction peak is shown to decrease while the lower side distributions are almost unchanged in the leading edge region. This must be attributed to the fact that near the section 3 the wake vorticity emitted from the blade tip is intense and strongly dependent on the azimuth ψ (see the radial flow maps of the propeller wake presented in references 12, 20). Even though these experimental trends are corroborated by the COHV prediction code, the calculated maximum negative peak value on the upper side is generally shifted towards the trailing edge at the two azimuthal blade positions considered.

The results presented above on the mean and instantaneous Cp distributions clearly indicated that significant instantaneous interaction effects have to be considered for a proper interference process modeling. Although good agreements between COHV calculation and experiment have been shown on the mean interference effects averaged over the rotational period, a better prediction of the instantaneous interference effects would be obtained by accounting for both the wake geometry deflection and the shearing of the slipstream due to the wing.

Conclusions

An experimental and numerical study of propeller wakes operating either in the isolated configuration or in the interacting propeller/nacelle/wing configuration of the axial flight regime has been pursued in this paper.

For the isolated propeller flowfield, the SMEHEL code based on a complete equilibrium procedure of the tip vortex and the inboard vortex sheet filaments have been checked by comparison with a detailed experimental data base. This calculation model has shown a good efficiency in predicting both overall propeller performances and local instantaneous 3D velocity field at different distances of the rotating plane. The SMEHEL model provides a realistic and detailed wake flow description suited for interference problem investigation.

The propeller/nacelle/wing interference problem has been experimentally simulated by means of a scaled wind tunnel configuration. For the range of

parameters explored $0.7 \leq \gamma \leq 1$; $\alpha = 0°$, the net slipstream influence on the fixed wing can be characterized as follows

1) a significant increase of the induced mean drag coefficient C_{Di} of the wing when compared to the uniform flow drag coefficient $C_{D\infty}$. A ratio of $C_{Di}/C_{D\infty}$ up to 5 has been measured at the maximum thrust value of the propeller (e. g. at low values of γ).

2) milder slipstream influences are exhibited on the mean induced lift and moment coefficients (C_{Li}, C_{Mi}) when compared to corresponding uniform flow coefficients of the wing ($C_{L\infty}$, $C_{M\infty}$).

Reciprocally the wing influence on the propeller performances has revealed an increase of the induced thrust and power coefficients. For the investigated range of parameters (α_0,γ), the mean induced effect is quantified by the following values $\tau_{ind} \approx 0.14\ \tau_{w/o\ wing}$ and $\chi_{ind} \approx 0.08\ \chi_{w/o\ wing}$

The numerical modeling of the slipstream influence on the wing has been undertaken by means of the COHV code based on the SMEHEL code associated with a panel method for the wing, and neglecting (as a first step) the influence of the wing on the slipstream. The COHV code efficiency has been also checked by comparison with experiments performed on the mean and instantaneous wing aerodynamics. Although the mean calculated pressure distribution has shown a good agreement with the experimental mean values, the actual version of the computer code COHV must be improved by considering the wake geometry deflection and the shearing of the slipstream due to the wing, and thus including the reciprocal influence of the wing on the propeller slipstream. Such improvements should provide a reliable tool for predicting the instantaneous interference effects on the propeller/nacelle/wing configuration.

Acknowledgement

The present research has been supported by the "Direction des Recherches Etudes et Techniques" under Grants No. 85/115 and 87/095.

References

1 Bousquet, J.M., "Méthodes aérodynamiques utilisées en France pour l'étude des hélices pour avions rapides", AGARD-FDP on Aerodynamics and Acoustics of Propellers, AGARD CP 366, paper N°2, Toronto, October 1984.

2 Lesieutre, D.J. and Sullivan, J.P., "Unsteady Forces on Counter-rotating propellers Blades", AIAA 4th Applied Aerodynamics Conference, AIAA paper 86-1804, San Diego, June 1986.

3 Kirmann, C., Rousseau, A. and Yermia, M., "Calcul du souffle moyen d'une hélice et de son influence sur les performances d'un avion", L'Aéronautique et l'Astronautique, Vol. 104, 1984-1, pp. 1-45.

4 Johnson, W., Lau, B.H. and Bowles, J.V., "Calculated Performance, stability and Maneuverability of High Speed Tilting-Prop-Rotor Aircraft", Proceedings of the 12th European Rotorcraft Forum Garmisch-Partenkirchen, September 1986.

5 Andres, J., Hubert, H. and Renaud, J., " The Tilt-Rotor Aircraft: a Response to the Future from European Interrogations to EUROFAR Actions", Proceedings of the 12th European Rotorcraft Forum Garmisch-Partenkirchen, September 1986.

6 Clark, D.R. and Mc Veigh, M.A., "Analysis of the Wake Dynamics of Typical-Rotor Configuration in Transition Flight", Proceedings of the 11th European Rotorcraft Forum, Paper N° 29, London, September 1985.

7 Ting, L., Liu, C.H. and Kleinstein, G., "Interference of Wing and Multipropellers", AIAA Journal, Vol. 10, N°7, 1972, pp. 906-914.

8 Rizk, M.H., "Propeller Slipstream/Wing Interaction in the Transonic Regime", Journal of Aircraft Vol. 18, N°3, March 1981, pp. 184-191.

9 Aljabri A.S. and Hughes, A.C., "Wind Tunnel Investigation of the Interaction of Propeller Slipstream with Nacelle/Wing/Flap Combinations", AGARD-FDP on Aerodynamics and Acoustics of Propellers, AGARD CP 366, paper N°21, Toronto, October 1984.

10 Sundar, R.M. and Sullivan, J.P., "An Experimental Investigation of Propeller Wakes using a Laser Doppler Velocimeter", AIAA 24th Aerospace Sciences Meeting, AIAA paper 86-0080, Reno, January 1986.

11 Favier, D. and Maresca, C., "Etude du Sillage 3D d'une Hélice Aérienne Quadripale", AGARD-FDP on Aerodynamics and Acoustics of Propellers, AGARD CP 366, paper N°15, Toronto, October 1984.

12 Favier, D., Nsi Mba, M., Barbi, C. and Maresca, C., " A Free Wake Analysis for Hovering Rotors and Advancing Propellers", VERTICA, Vol. 11, N° 3, 1987, pp. 493-511.

13 Graber, A. and Rosen, A., "A parametric Investigation of a Free Wake Analysis of Hovering Rotors", Proceedings of the 12th European Rotorcraft Forum, Paper N° 22, Garmisch-Partenkirchen, September 1986.

14 Chen, C.S., Velkoff, H.R. and Tung, C., "Free-Wake Analysis of a Rotor in Hover", AIAA 19th Fluid and Plasma Dynamics Conference, AIAA paper 87-1245, Honolulu, June 1987.

15 Steinhoff, J. and Ramachandran, K., "A Vortex Embedding Method for Free Wake Analysis of Helicopter Rotor Blades in Hover", Proceedings of 13th European Rotorcraft Forum, Paper No. 11, Arles, September 1987.

16 Howard, R.M., Miley, S.J. and Bruce, J.H., "An Investigation of the Effects of the Propeller Slipstream on the Laminar Wing Boundary Layer", General Aviation Aircraft Meeting and Exposition, paper N°850859, Wichita, April 1985.

17 Welge, H.R. and Crowder, J.P., "Simulated Propeller Slipstream Effects on a Supercritical Wing", NASA CR-15138, June 1978.

18 Ettaouil, A., "Etude Numérique du Champ Aérodynamique d'une Hélice Aérienne Isolée ou en Interaction avec une Voilure-Validation par Comparaison avec l'Expérience." Thèse de Doctorat de l'Université Aix-Marseille II, N°207.208.87.24, Septembre 1987.

19 Favier, D., Maresca C. and Nsi Mba, M.,"Etude de l'Interaction Souffle d'Hélice/Voilure et Etude du Champ Aérodynamique d'un Rotor d'Hélicoptère en Vol Stationnaire et en Vol d'Avancement", Rapport D.R.E.T. n° 85/115, Décembre 1987.

20 Favier, D., Maresca, C., Nsi Mba, M. and Barbi, C., "Experimental and Numerical Aerodynamic Study of Rotors and Propellers Operating in Several Flight Conditions", Proceedings of 2nd International Conference on Basic Rotorcraft Research, College Park, University of Maryland, February 1988.

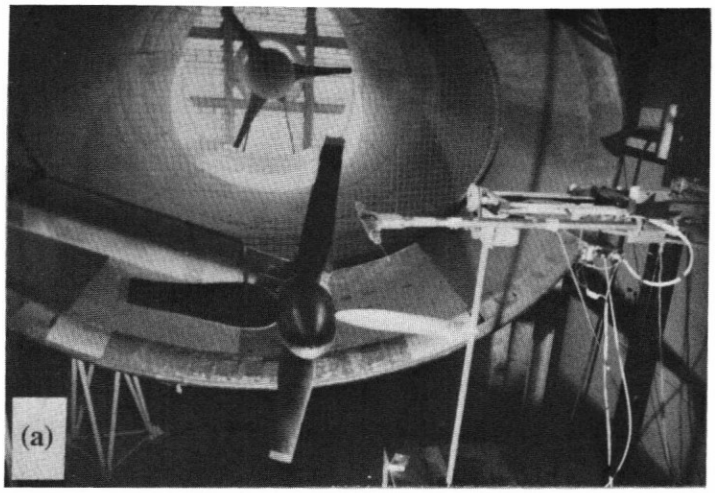

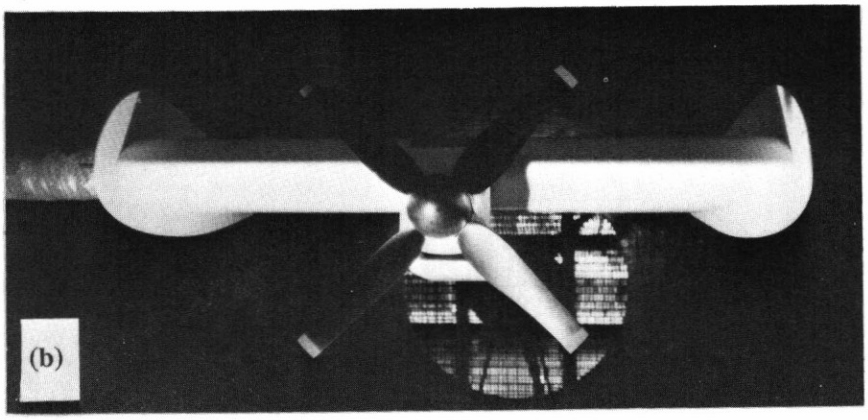

Fig. 1a,b Views of the wind tunnel set up from upstream of the model: (a) isolated propeller; (b) propeller/nacelle/wing.

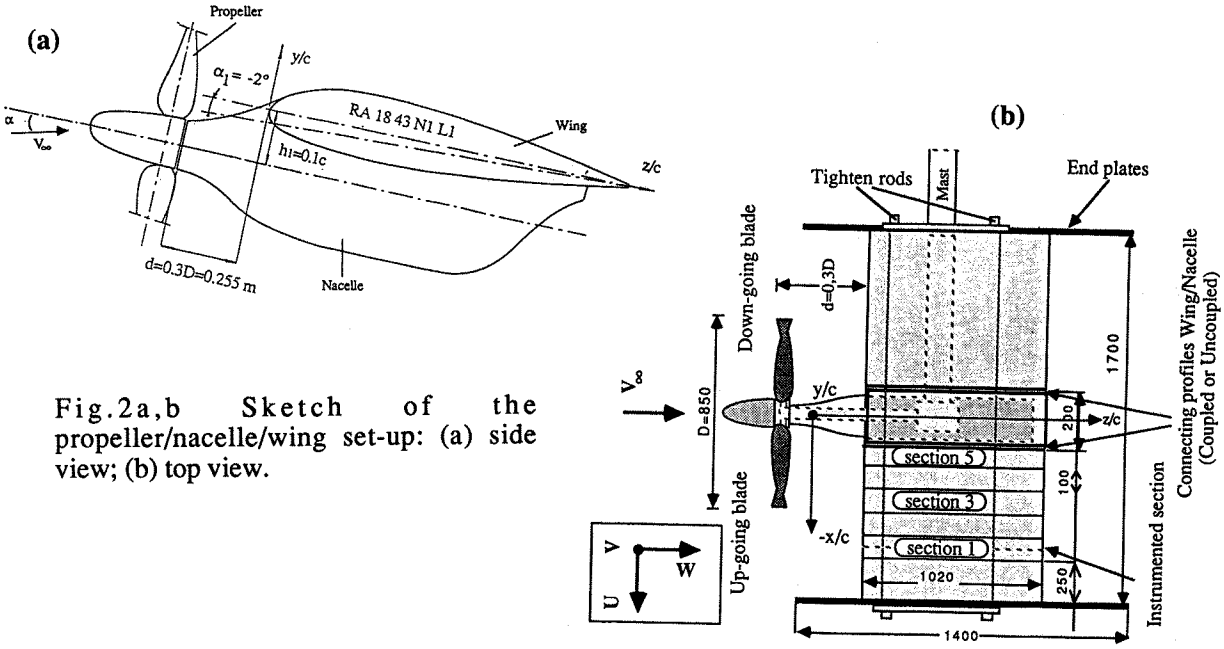

Fig.2a,b Sketch of the propeller/nacelle/wing set-up: (a) side view; (b) top view.

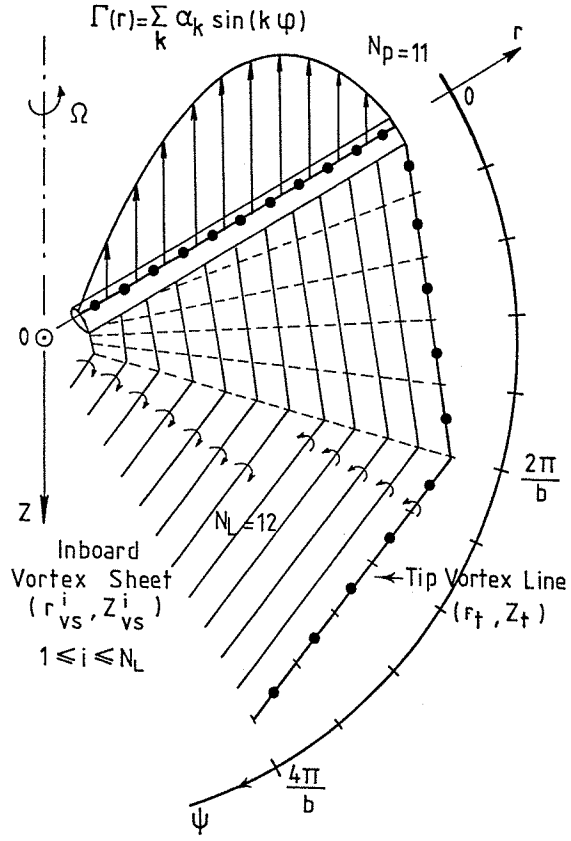

Fig. 3 Blade and wake representations for FWA model in axial flight.

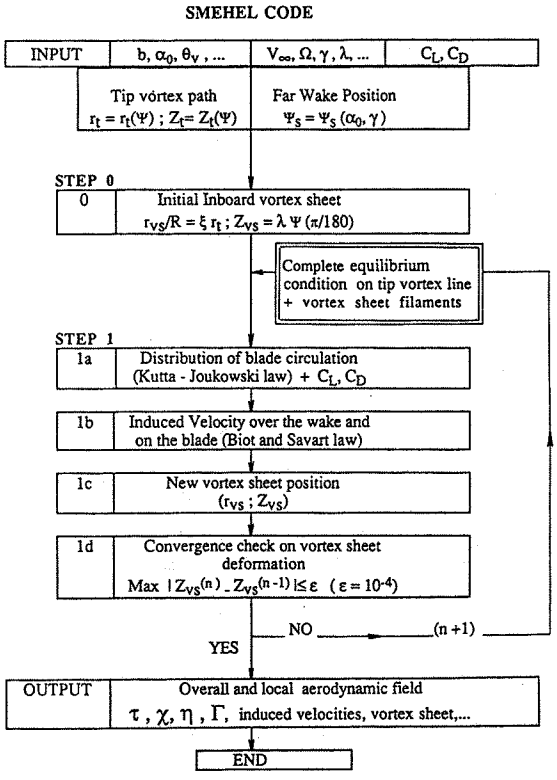

Fig. 4 SMEHEL block diagram based on a complete equilibrium procedure.

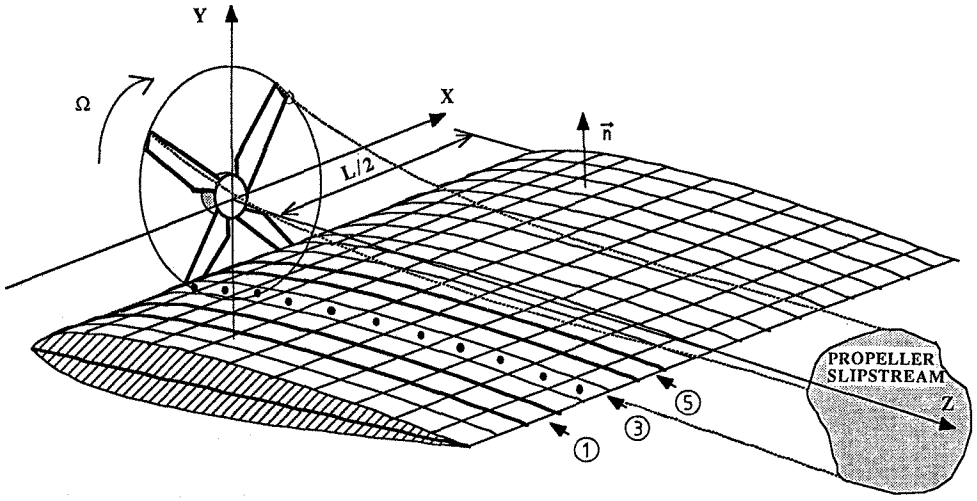

Fig. 5 Slipstream and wake representations for the coupling model COHV.

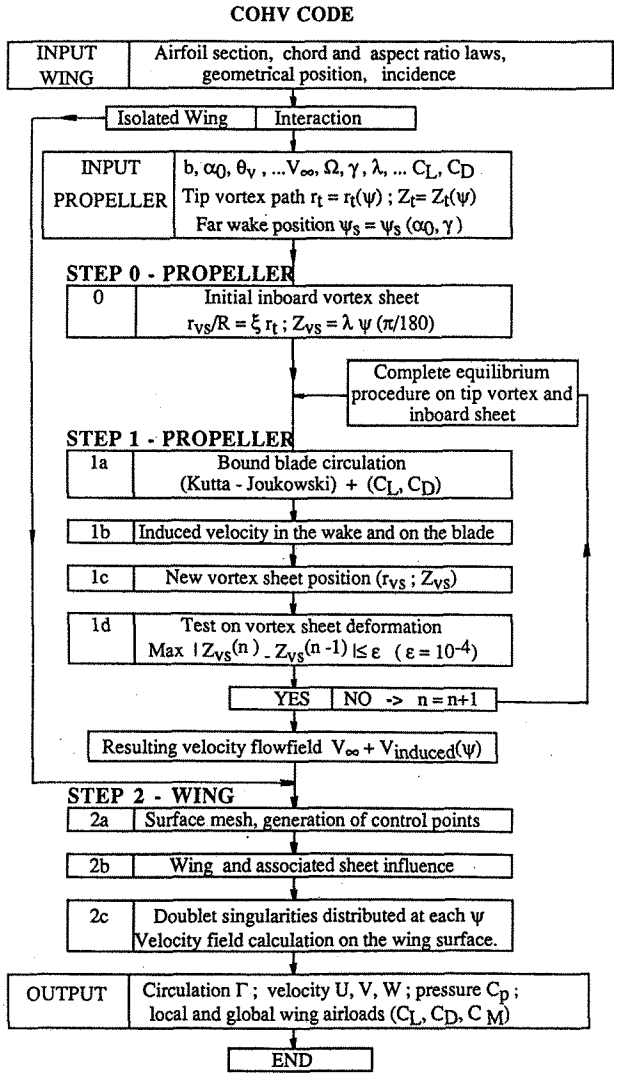

Fig. 6 COHV Block diagram based on calculation of the slipstream influence on the wing.

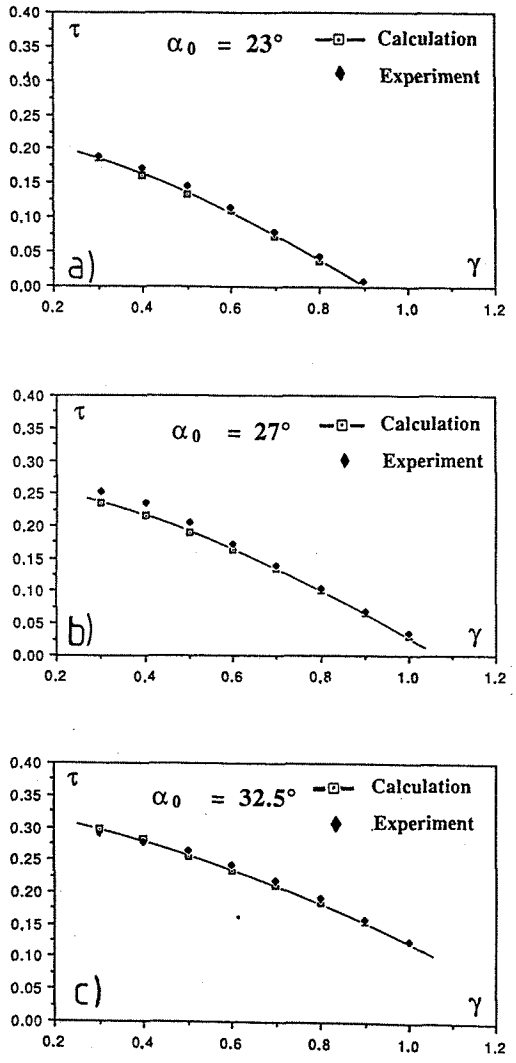

Fig. 7 a,b,c SMEHEL calculation results versus experiments on the thrust coefficient τ of the isolated propeller.

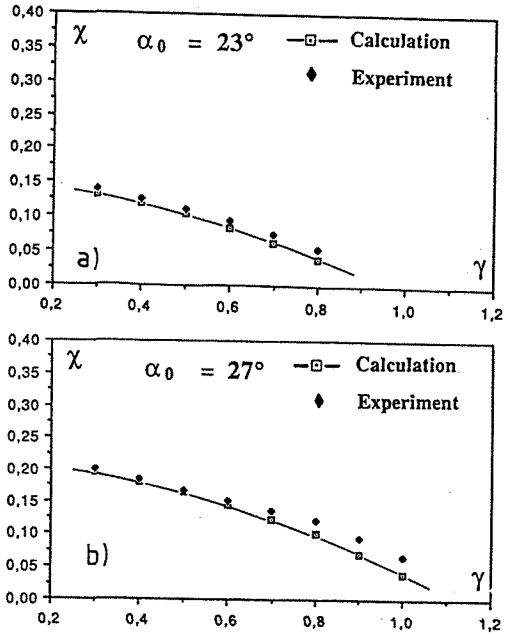

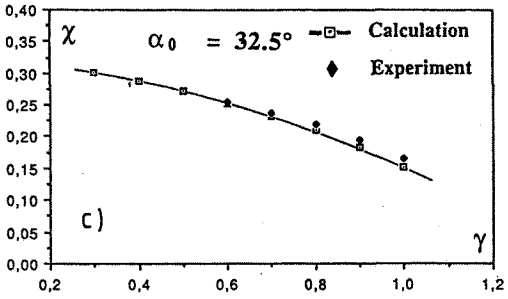

Fig. 8 a,b,c SMEHEL calculation results versus experiments on the power coefficient χ of the isolated propeller.

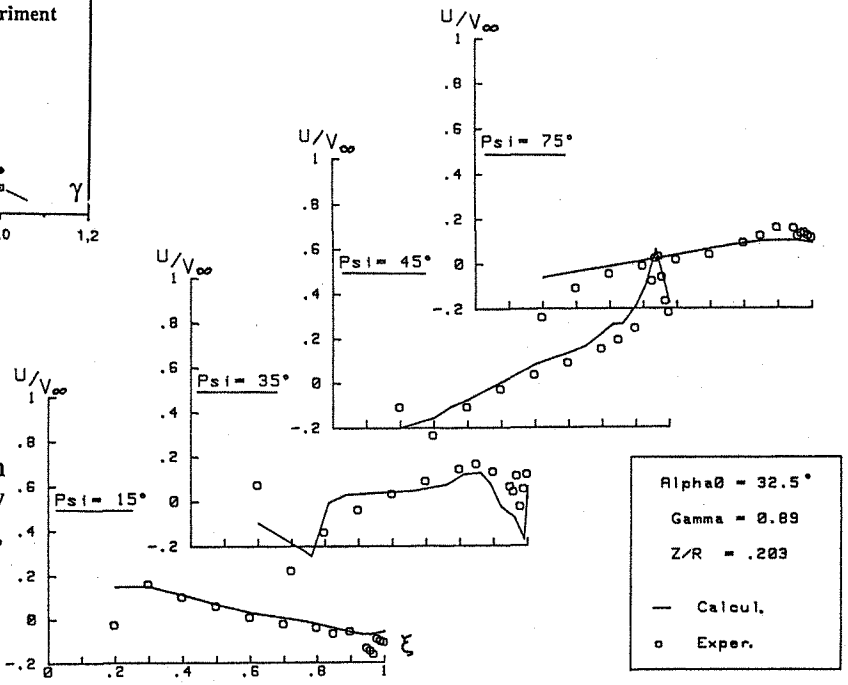

Fig. 9 Comparison calculation /experiment on the radial velocity component $U=U(r,\psi)$ at $\gamma = 0.89$, $\alpha_0 = 32.5°$, $Z/R = 0.203$.

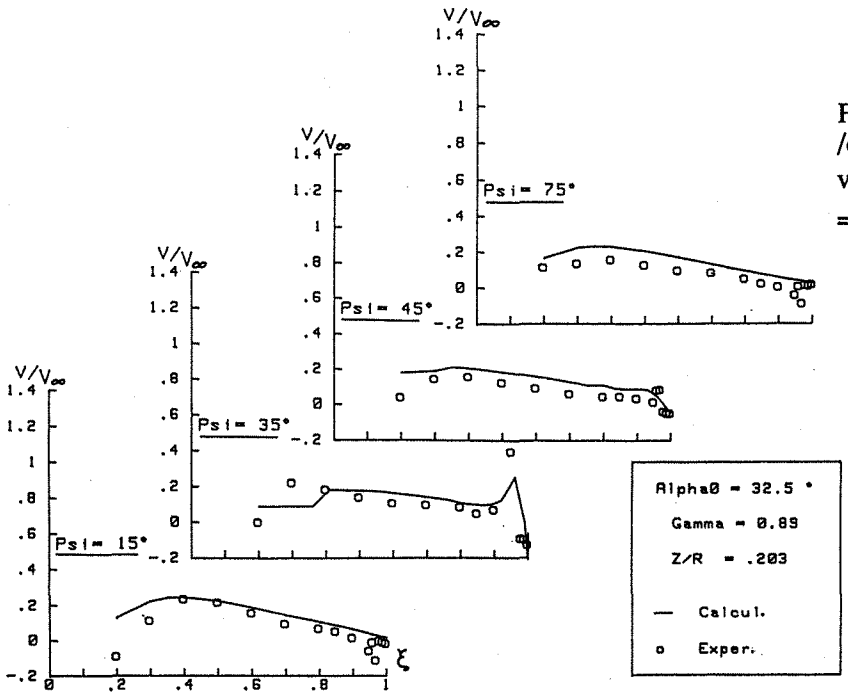

Fig. 10 Comparison calculation /experiment on the tangential velocity component $V=V(r,\psi)$ at $\gamma = 0.89$, $\alpha_0 = 32.5°$, $Z/R = 0.203$.

Fig. 11 Comparison calculation/experiment on the axial velocity component W=W(r,ψ) at $\gamma = 0.89$, $\alpha_0 = 32.5°$, Z/R = 0.203.

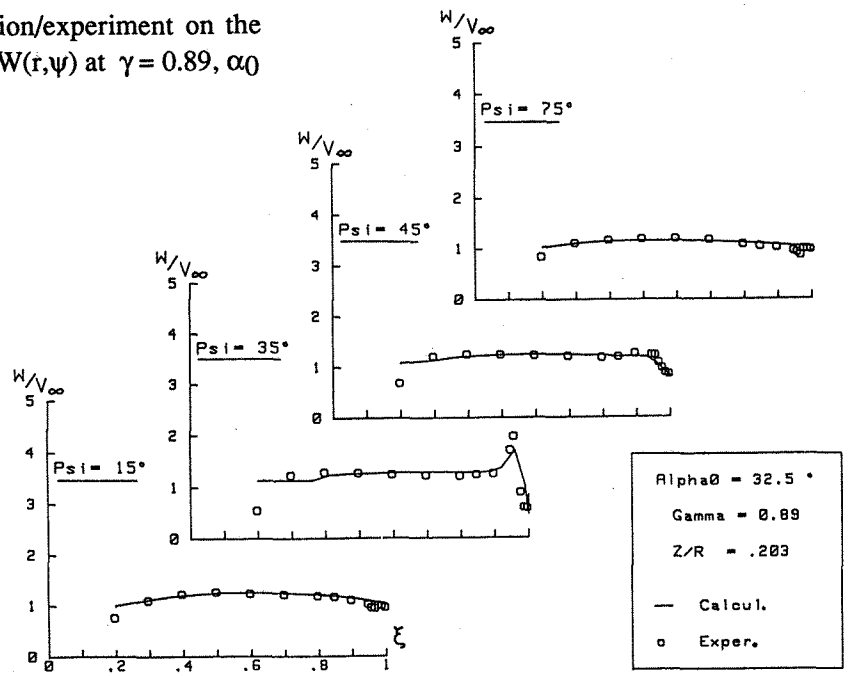

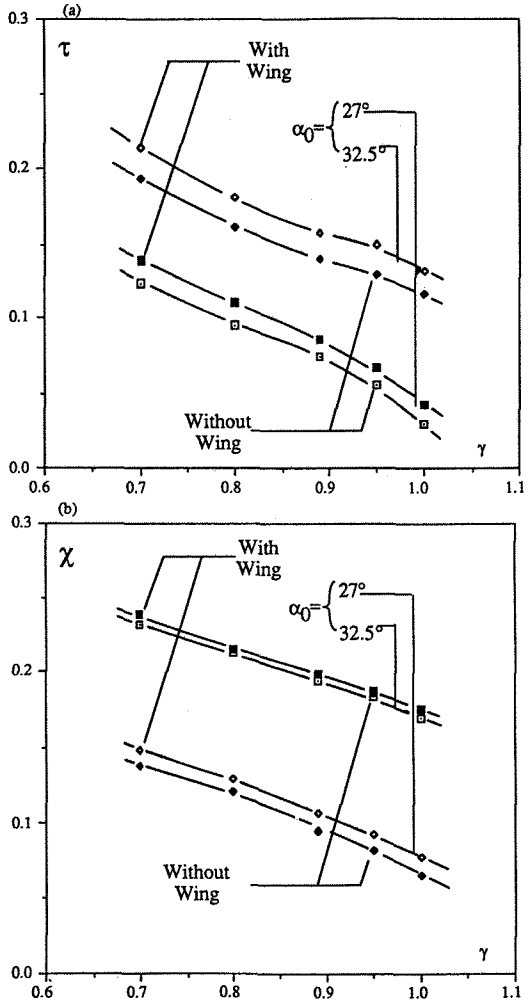

Fig. 12 a,b Wing influence on the propeller performances: (a) Thrust coefficient $\tau = \tau(\gamma)$; (b) Power coefficient $\chi = \chi(\gamma)$.

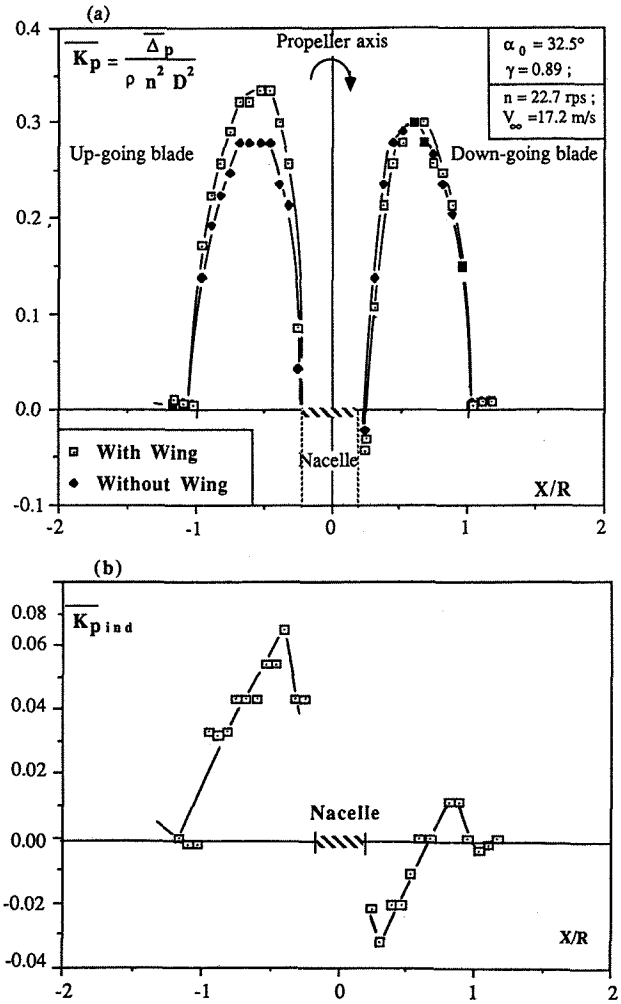

Fig. 13 a,b Mean total pressure jump through the propeller disk: (a) with and without the wing; (b) net induced effect.

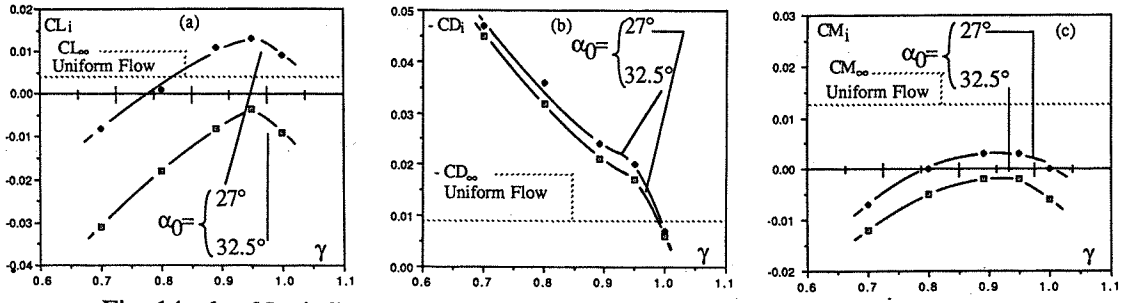

Fig. 14 a,b,c Net influence of the slipstream on the wing as a function of γ : (a) induced lift coefficient C_{Li}; (b) induced drag coefficient C_{Di}; (c) induced moment coefficient C_{Mi}.

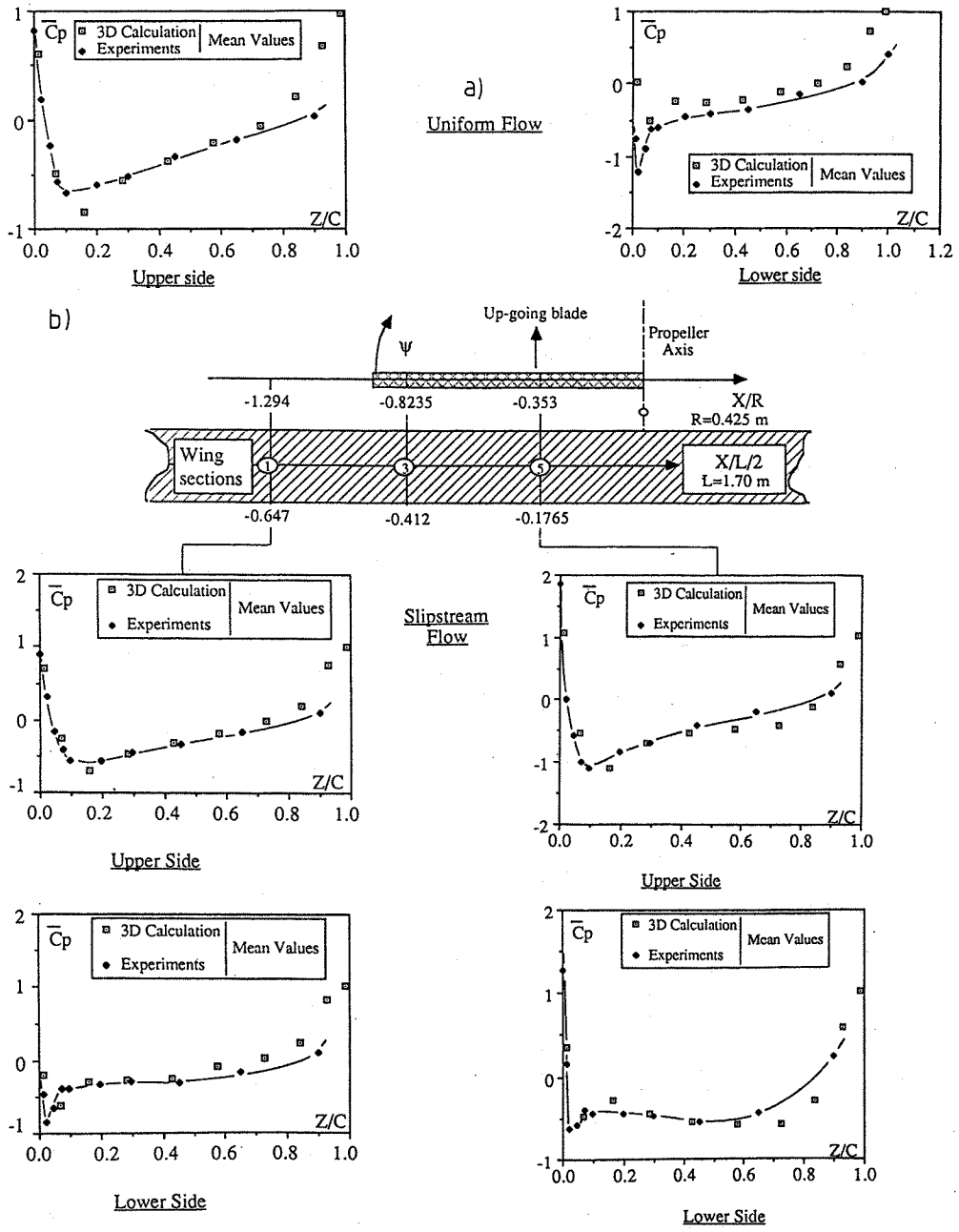

Fig. 15 a,b Comparison calculation/experiment on the mean pressure $\overline{C_p} = \overline{C_p}(Z)$ along of the wing span: (a) without the slipstrean ; (b) with the slipstrean.

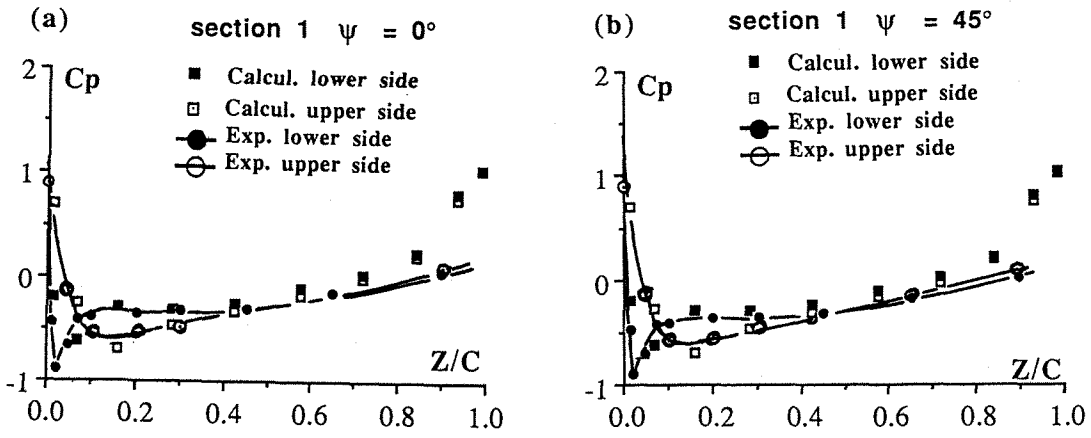

Fig. 16 a,b Comparison calculation/experiment on the instantaneous pressure distributions Cp=Cp(Z) at X/(L/2) = - 0.65 (section 1): (a) $\psi = 0°$; (b) $\psi = 45°$.

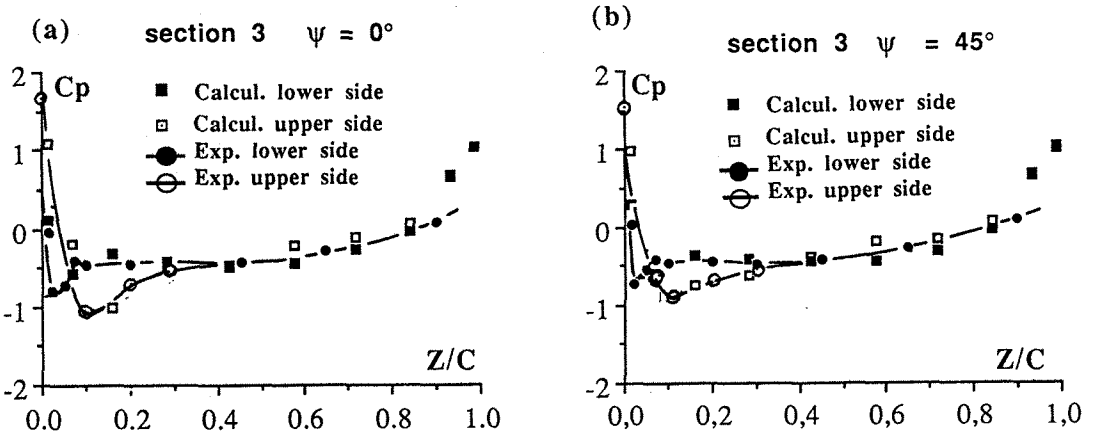

Fig. 17 a,b Comparison calculation/experiment on the instantaneous pressure distributions Cp=Cp(Z) at X/(L/2) = - 0.41 (section 3): (a) $\psi = 0°$; (b) $\psi = 45°$.

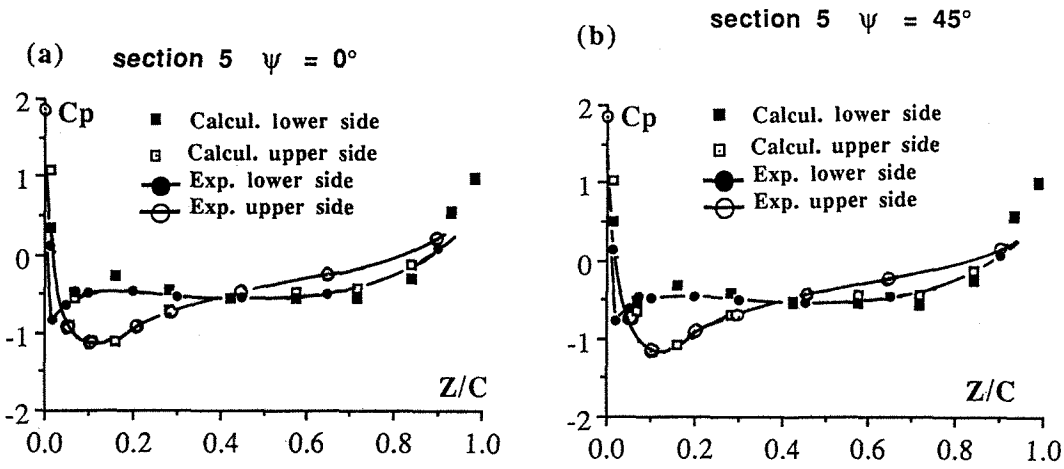

Fig. 18 a,b Comparison calculation/experiment on the instantaneous pressure distributions Cp=Cp(Z) at X/(L/2) = - 0.18 (section 5): (a) $\psi = 0°$; (b) $\psi = 45°$.